AAS 23-226

A BACK-PROPAGATED EFFORT METRIC FOR MANEUVERING SPACE OBJECTS CORRELATION

Riccardo Cipollone*, Pierluigi Di Lizia†

Correlation is one of the first steps of Space object catalog maintenance, aimed at understanding whether a known target generated an acquired measurement. Statistical distance-based approaches are not always enough when dealing with controlled objects, leading to alternative correlation metrics that exploit the effort of linking the track to candidate orbits. This work describes a novel optical measurement correlation tool, exploiting optimal control theory to back-propagate an admissible region of observables to catalog epochs through a patchwork of Taylor polynomial expansions. The resulting minimum expense distributions are combined with a standard statistical distance to support the correlation of maneuvering objects.

INTRODUCTION

The overcrowded status of the near-Earth environment represents a progressively more urgent issue both Space agencies and companies are well-aware of. Due to diverse reasons, mostly linked to a generally increased probability of intertwined collisions and fragmentations, the Resident Space Objects (RSO) spanning across every operational orbital regime are very likely to affect and hamper every phase composing both the design of a new mission and its deployment, from launch to end-of-life. This increasing concern has led to the spread of dedicated hardware and software solutions to monitor the evolution of the RSO population and to mitigate its effects on new and ongoing missions. The final aim of these activities is to achieve a continuous Space Domain Awareness (SDA) being as comprehensive as possible of the current picture. In this specific framework, Space Surveillance and Tracking (SST) is one way of monitoring Space objects, coordinating international sensor networks to acquire measurements and processing them to retrieve orbital information. Some by-products of this process are ESA's Annual Space Environment Report[1] , aimed at regularly assessing the severity of the situation in terms of debris population trends and figures, and the publicly available RSO catalog in Space-Track website*, provided and maintained by the US Combined Force Space Component Command (CFSCC). The pipeline behind catalog updates starts with one or more new acquisitions, processed into measurements of different kinds, according to the sensor. A first correlation process between the uncorrelated tracks (UCTs) takes place to cluster them if they are identified as belonging to the same target. They are then scanned for correlation with cataloged objects. In case of success, the target orbit is updated by means of a Refined Orbit Determination process while a second scan on the active spacecraft subset of the catalog can be performed otherwise to consider a maneuver hypothesis. If this step fails as well, the last resort is an Initial Orbit

*Ph.D. student, Department of Aerospace Science and Technology, Via Giuseppe La Masa 34, Milan, Italy.
†Associate Professor, Department of Aerospace Science and Technology, Via Giuseppe La Masa 34, 20156, Milan, Italy.
*https://www.space-track.org

Determination (IOD) process, given that enough UCTs are available. In this way, a first orbit estimate is obtained from the only observables and stored so that the unknown target can be observed again.

When it comes to operational objects, maneuver detection and characterization play a key role in the measurement processing chain. Even if the purpose of every method developed in this field is clear, there are different levels according to which they can be categorized, the most high-level one being the knowledge of the observed target: methods deeply differ depending on it being cataloged (or even cooperative) or unknown. The former case covers detection aimed at characterizing a target's pattern of life, leveraging past orbital data to provide history-based information to be integrated into robust tracking and estimation algorithms. The latter instead implies a deep link to the initial phases of an SST pipeline, involving both the UCT-to-UCT association and the UCT-to-orbit one. The objective is to assist standard correlation techniques, usually relying on statistical distribution distances as metrics to compute an index and rank the available candidates. The main line of research on this second aspect identifies the effort associated with the maneuver to link the candidate couple as a suitable figure to retrieve an alternative correlation index for operational targets. One of the first works in this direction is the one by M.K. Holzinger et al.[2] , where a first formulation of an effort metric is proposed as the velocity expense associated with the solution of a minimum-energy low-thrust Optimal Control Problem (OCP). The optimality hypothesis is a strong but reliable criterion because of the high costs associated with fuel in a Space mission context making at the same time the metric suitable for non-maneuvering targets too. Besides, choosing the minimum-energy low-thrust version of the problem deliberately overestimates the minimum effort required to connect the boundary conditions (BCs), resulting in a reasonable trade-off. The effort metric concept has thereby evolved and different techniques have enriched its state of the art. An impulsive version is reported by A. Pastor et al.[3] , linking an orbit to an optical track by means of a single-burn impulsive maneuver and two orbits using a double-burn impulsive one. Optimality is assumed in this case too, leading to an optimization process of the velocity expense ΔV, linearly mapped to perturbations of the final track (or state). A minimum-energy OCP is formulated by J.A. Siminski et al.[4] to link a known orbit to a new optical track, in the form of an attributable (concatenation of the target angles and angular rates), by constraining an Admissible Region[5] (AR) to a maximum ΔV expense and embedding a data-driven probability density function of orbital parameters variations in the process. An alternative approach in this direction is presented by Serra et al.[6] , where optical tracks are correlated by means of a Taylor polynomial expansion of a minimum-energy low-thrust OCP around a reference trajectory (solution of the nominal OCP), exploiting a constrained AR to limit the observable space in which to search for the minimum.

The work described in this paper stems from this last research path, tailoring the maneuver hypothesis and detection step to the pipelines scanning cataloged objects for correlation. A novel method is thus proposed to both define suitable candidates for optical UCTs correlation and detect whether they have been subject to active control. By exploiting Taylor Differential Algebra (TDA) and an Automatic Domain Splitting (ADS) technique, a set of minimum-energy OCP solution Taylor polynomial expansions is defined to sample a constrained AR. The propagation flow runs back in time propagating the entire AR to the candidate epochs. In this way, the number of integrations needed to scan the catalog is converted to the one required to properly map the whole AR back to every given epoch. The method is able to provide a first ranking of the candidate objects by retrieving the minimum thrust energy expense and its coordinates in terms of range and range rate. BCs uncertainty is embedded in the process thanks to TDA formulation itself, allowing for the definition

of the expense distributions used to define a robust metric.

MATHEMATICAL TOOLS

This section covers the theoretical basis of the approach. Firstly, a brief introduction to the minimum-energy OCP formulation for the case at hand is provided together with some insights on the AR definition and the boundaries used to further constrain it. Therefore, a description of TDA fundamentals and their relationship to the ADS process is provided.

Minimum-Energy Optimal Control Problem setup

Two main sources of information are involved in a UCT-to-orbit correlation framework, composing the problem BCs. On the one hand, the catalog of RSOs is used as a pool to search for suitable candidates, each one represented by its last orbital state and corresponding epoch. On the other hand, the incoming measurement, according to the nature of the sensor, gives a partial or complete description of an orbital state at observation epoch. The complete set required to uniquely characterize the orbital state is composed of range (ρ) range-rate ($\dot{\rho}$), angles (α, δ), and their time derivatives ($\dot{\alpha}, \dot{\delta}$). The equations connecting them to the state, assuming Earth-Centered Inertial (ECI) reference frame coordinates and Right Ascension and Declination as angles, are:

$$\begin{aligned} \mathbf{r} &= \mathbf{R}_s + \rho\,\mathbf{s} \\ \mathbf{v} &= \mathbf{V}_s + \dot{\rho}\,\mathbf{s} + \rho\,\dot{\mathbf{s}} \\ \mathbf{s} &= (\cos\alpha\,\cos\delta, \sin\alpha\,\cos\delta, \sin\delta) \end{aligned} \tag{1}$$

where $\mathbf{r}$ is the target position in ECI, $\mathbf{v}$ its velocity, $\mathbf{R}_s$ and $\mathbf{V}_s$ the ground station position and velocity and $\mathbf{s}$ the line-of-sight unit vector. In the case at hand, the focus is on optical measurements in the shape of an attributable $\mathbf{a} = (\alpha, \delta, \dot{\alpha}, \dot{\delta})$, resulting from a fitting process of a sequence of observed angles, whose sampling and time span can deeply affect the quality of the measurement itself. Given one available attributable, the observed state can be only partially defined, becoming a function of the missing observables $\rho, \dot{\rho}$.

To link these two BCs, the optimality assumption is inherited from the state of the art. Not only is it deemed reliable because of the tendency to save fuel to perform any kind of operation, but also due to the ultimate objective of correlation itself, that is to find associations through trajectories (and corresponding expenses) that are usually close to ballistic motion. In this way, even non-operational targets can be included in the analysis, their control action being the one derived from the only BCs uncertainty. An energy-optimal OCP is thus chosen and its cost is expressed as a thrust energy:

$$J = \int_{t_i}^{t_f} \frac{1}{2}\mathbf{u}(\tau)^T\mathbf{u}(\tau)\,d\tau \tag{2}$$

Where $\mathbf{u}(t)$ is the acceleration profile while t_i and t_f define the initial and final epoch respectively.

Despite the optimality assumption, this cost index represents a conservative option, due to the fact that it is proven to constitute an upper bound on the equivalent fuel-optimal OCP solution $\Delta V_f = \int_{t_i}^{t_f} ||\mathbf{u}(\tau)||_2\,d\tau$, by enforcing Chauchy-Schwartz inequality. In addition, the fuel-optimal ΔV_f bounds the impulsive OCP from above due to the infinite acceleration magnitudes involved in the latter, making the minimum-energy low-thrust choice the most expensive of the three.

The resulting OCP formulation is:

$$\min_{\mathbf{u}(\tau)} J = \int_{t_i}^{t_f} \frac{1}{2}\mathbf{u}(\tau)^T\mathbf{u}(\tau) \quad \text{s.t.} \begin{cases} \dot{\mathbf{x}} = \mathbf{f}(t, \mathbf{x}(t), \mathbf{u}(t)) \\ \mathbf{x}(t_i) = \mathbf{x}_i \\ t_i, t_f \text{ given} \end{cases} \tag{3}$$

Where $\mathbf{x}_i$ stands for the state at initial time t_i and $\dot{\mathbf{x}}(t) = \mathbf{f}(t, \mathbf{x}(t), \mathbf{u}(t))$ represents the problem's dynamics.

The OCP is solved by leveraging an indirect formulation, augmenting the state with an adjoint one $\boldsymbol{\lambda}$ to obtain a Two-Point Boundary Value Problem (TPBVP). Assuming affine control, and defining the Hamiltonian as $\mathcal{H} = l(t, \mathbf{x}(t), \mathbf{u}(t)) + \boldsymbol{\lambda}(t)^T\mathbf{f}(t, \mathbf{u}(t), \mathbf{x}(t))$ (where $l = \frac{1}{2}\mathbf{u}^T\mathbf{u}$), the null Hamiltonian derivative with respect to the control provides the relation $\mathbf{u}(t) = -\mathbf{B}\boldsymbol{\lambda}(t)$ (where $\mathbf{B}$ is a constant coupling coefficient), while its partial derivatives with respect to the adjoint state $\mathcal{H}_\lambda$ and state $\mathcal{H}_\mathbf{x}$ define the TPBVP equations (dependencies are dropped for the sake of clarity):

$$\begin{cases} \dot{\mathbf{x}} = \mathcal{H}_{\boldsymbol{\lambda}} \\ \dot{\boldsymbol{\lambda}} = -\mathcal{H}_{\mathbf{x}} \\ \mathbf{x}(t_i) = \mathbf{x}_i \\ \boldsymbol{\lambda}(t_f) = \boldsymbol{\lambda}_f \end{cases} \tag{4}$$

The initial value for $\boldsymbol{\lambda}(t)$ has to be retrieved to solve the problem, leading to the target continuous control profile and the corresponding energy expense by integration in time.

Given the BCs of an optical track correlation ($\mathbf{x}_i$ completely described, $\mathbf{x}_f(\rho, \dot{\rho})$), there are two ways to exploit them to solve the TPBVP and find the optimal expense. The former enforces transversality conditions, taking the only observables available into account to obtain an optimal solution, while the latter is based on a nested optimization process, finding the minimum optimal expense across a search space defined in the missing observables' space. In this case, the second method is employed to provide a complete description of the state at final time, by expressing it as a function of ρ, $\dot{\rho}$:

$$\min_{\rho,\dot{\rho}} J(\mathbf{x}_i, \mathbf{x}_f(\rho, \dot{\rho}), \mathbf{u}^*(t)) \tag{5}$$

where $\mathbf{u}^*(t)$ is an optimal control profile, given a set of BCs.

This choice is mainly driven by the reduced number of optimization variables involved, granting an easier interaction with the domain-splitting process and a direct link with the AR formulation.

Constrained Admissible Region

The original AR formulation by A. Milani[5] has been further developed by DeMars[7] with the definition of strict constraints stemming from the orbital regime of interest. More specifically, semi-major axis a and eccentricity e are expressed as a function of range and range rate:

$$
\begin{aligned}
-\frac{\mu}{2(\frac{v^2}{2}-\frac{\mu}{r})} - \bar{a} &= 0 \\
\left\| \frac{\mathbf{v}\times\mathbf{h}}{\mu} - \frac{\mathbf{r}}{r} \right\| - \bar{e} &= 0
\end{aligned}
\tag{6}
$$

where μ is the Earth gravitational parameter, $\bar{a}$ and $\bar{e}$ identify the boundary semi-major axis and eccentricity and $\mathbf{h}$ is the specific angular momentum. $\mathbf{r}$ and $\mathbf{v}$ represent the state position and velocity (r and v being their norm) and they can be easily expressed as a function of ρ and $\dot{\rho}$ by means of Eq. 1. These equations can be used as constraints by setting (in the case of Earth-bound RSOs) a maximum and minimum value for the semi-major axis and a maximum value for eccentricity. These constraints can be conveniently employed to restrain the search space in case the target set of operational objects is known to cover a specific orbital region.

Taylor Differential Algebra

The basic concept behind TDA is the conversion of numerical problems into an approximate analytical counterpart by means of progressive composition of Taylor Truncated Power Series (TPA) as reported by A. Witting.[8] Given a function f of v variables that is $\mathcal{C}^{(k+1)}$ in the domain of interest $[-1,1]^v$ (scaled as required by the problem at hand), a TDA transform can be applied, converting it to a polynomial expansion around a reference value x_0, truncated to an arbitrary order N:

$$
f(x) = \sum_{k=0}^{N} \frac{f^{(k)}(x)}{k!}(x-x_0)^k \tag{7}
$$

This formulation allows for the definition of results that are typically iteration-driven to be retrieved as an equivalent function evaluation. The clearest examples are numerical integration schemes, whose flow can be condensed in a single function evaluation thanks to the recurrent TPS composition at each of its steps. The basic unit of TDA resides in the definition of a variable $[x]$ as comprised of two parts: a constant one $\bar{x}$, linked to the expansion center, and a perturbed term δx, related to the expansion. Every operation performed on this kind of variable generates results featuring the same structure, including a reference and the related expansion.

The library used to apply TDA to the current method is the C++ Differential Algebra Core Engine* (DACE), defining a DA variable type through the coefficients of the underlying expansion. This type allows for easier computation of gradients, derivatives, and integrals of function TDA approximations as well as root-finding and optimization techniques using a fixed-point polynomial inversion algorithm[9] as their core.

There are two main aspects to focus on to obtain a reliable approximation of a given function with this tool. The former consists in assessing how well the TPS approximation follows the real function non-linearities. This kind of analysis can be performed by monitoring the truncation error associated with the TPS by enforcing Taylor's theorem[8] . Consequently, given a TPS of order N, the magnitude of the $N+1$ term provides hints about the need to increase or decrease the expansion order of the polynomial map to better fit the real function. The latter aspect is instead the stability of the map across the domain of interest. High orders of expansion can lead to instability at its boundaries and polynomial inversion algorithms can diverge for the same reason. These two issues

*`https://github.com/dacelib/dace`

are the main reasons why domain-splitting techniques are employed to cover large domains, given a target truncation error and expansion order.

Automatic Domain Splitting

The ADS technique employed in this work leverages Taylor's theorem to decrease the truncation error of a polynomial map over an initial domain by splitting it iteratively. Its working principle is based on the fact that bisecting the original domain causes the error's upper bound on the new domains to shrink by a factor of 2^{N+1}, amplified by the expansion order N. The split, from a practical point of view, consists of a remapping of the initial domain $\mathcal{D}$ in the two subdomains $\mathcal{D}_{x_i,1}$ $\mathcal{D}_{x_i,2}$ across the selected direction i with the following linear functions:

$$\begin{aligned} \mathcal{D}_{x_i,1}(x) &= \frac{1}{2}\,x + \frac{1}{2} \\ \mathcal{D}_{x_i,2}(x) &= \frac{1}{2}\,x - \frac{1}{2} \end{aligned} \tag{8}$$

Doing this recursively results in a bisection method aimed at reaching a target accuracy, the main drawback being the integrations required for the definition of new centers of expansion at each iteration.

Even if the rationale for this technique is the same, the strategies to efficiently implement it are diverse. The algorithm selected for this tool[10] selects when the expansion needs to be split according to the L-infinity norm of the $N+1$ terms of the expansion. As for the split direction in the case of a multivariate function, the choice is based on a refactoring of the polynomial, performed for every x_i variable of $\mathbf{x} \in \mathbb{R}^v$ as follows:

$$P(\mathbf{x}) = \sum_{k=0}^{N} x_i^k c_{i,k}(x_1, x_2, ..., x_{i-1}, x_{i+1}, ...x_v) \tag{9}$$

Where $c_{i,k}$ is the k-order term coefficient of the i-th variable. The $N+1$ term L-infinity norm is then computed for each refactoring and the variable corresponding to the highest one is selected as the splitting direction.

METHOD

This section details the steps followed to build the pipeline, from dynamics back-propagation to the TPS linking perturbations in thrust energy expense ΔE to the ones in ρ and $\dot{\rho}$. Therefore, the optimization and the uncertainty integration steps are described as well as the selected correlation and maneuver detection test metrics.

Backwards dynamics

Traditional correlation pipelines often involve the computation of a statistical distance between candidate known objects and one or more new measurements. This distance is usually computed at observation time, projecting the propagated candidate state onto the measurement space. This procedure implies a large number of propagations, given the typical size of an RSO catalog. Not only does this affects the required computational power, forcing a trade-off between processing time and dynamics model fidelity, but it also leads to the propagation of typically inaccurate TLE

(Two-Line Element) state uncertainties. Both these aspects can deeply affect correlation statistical significance. A way to address these shortcomings could be a single propagation of a measurement-derived state distribution at the observation epoch back to every correlation candidate epoch. Nevertheless, this state would derive from available observables (and their accuracy) and its complete description would depend on the sensor type. In the case at hand, this concept is leveraged by the definition of a bounded AR, sampled through TDA to map the corresponding orbital state manifold, and back-propagated to retrieve it at target epochs. The dynamics is thus a time-reversed version of the Keplerian Two-Body Problem with the adjoint state $\boldsymbol{\lambda}$ of Eq. 4, where every equation and time dependency gets a negative sign as in $\dot{\mathbf{x}} = -\mathbf{f}(-t, \mathbf{u}, \mathbf{x})$.

TDA setup

The ultimate aim of the following steps is to retrieve a polynomial map of the optimal thrust energy ΔE as a function of BC perturbations. A single candidate object case is considered as a baseline to better explain the steps of the algorithm, but the tool is meant to generate a solution thrust energy expense $\Delta E_n(\delta\rho, \delta\dot{\rho})$ for every n-th candidate object and epoch.

After the initialization of $[\rho]$, $[\dot{\rho}]$ and $[\boldsymbol{\lambda}_f]$ variables to expansion order 4, the polynomial map $\mathcal{M}$ is obtained by composition of the measurement-to-state one $\mathcal{H}$, embedding Eq. 1, and the back-propagation flow $\mathcal{P}$, as follows:

$$\begin{aligned} \delta\mathbf{x}_f &= \mathcal{H}(\delta\rho, \delta\dot{\rho}) \\ \begin{bmatrix} \delta\mathbf{x}_i \\ \delta\lambda_i \end{bmatrix} &= \mathcal{P}(\delta\mathbf{x}_f, \delta\boldsymbol{\lambda}_f) \\ \begin{bmatrix} \delta\mathbf{x}_i \\ \delta\lambda_i \end{bmatrix} &= \mathcal{M}(\delta\rho, \delta\dot{\rho}, \delta\boldsymbol{\lambda}_f) \quad \text{with } \mathcal{M} = \mathcal{P} \circ \mathcal{H} \end{aligned} \tag{10}$$

The expansion center corresponds to the ballistic trajectory, given a first guess of ρ_0, and $\dot{\rho}_0$ at t_f. This implies that any optimal $\delta\boldsymbol{\lambda}_f^*$ coincides with the actual optimal adjoint state $\boldsymbol{\lambda}_f^*$, the same holding for thrust energy perturbations and the actual expense ΔE.

A polynomial inversion strategy is then applied on $\mathcal{M}$ to obtain $\boldsymbol{\lambda}_f$ as function of ρ, $\dot{\rho}$ and $\mathbf{x}_i$ perturbations[11] :

$$\begin{aligned} \begin{bmatrix} \delta\mathbf{x}_i \\ \delta\rho \\ \delta\dot{\rho} \end{bmatrix} &= \begin{bmatrix} \mathcal{M}_x(\delta\boldsymbol{\lambda}_f, \delta\rho, \delta\dot{\rho}) \\ \mathcal{I}(\delta\rho, \delta\dot{\rho}) \end{bmatrix} = \mathcal{S}(\delta\boldsymbol{\lambda}_f, \delta\rho, \delta\dot{\rho}) \\ \begin{bmatrix} \delta\boldsymbol{\lambda}_f \\ \delta\rho \\ \delta\dot{\rho} \end{bmatrix} &= \mathcal{S}^{-1}(\delta\mathbf{x}_i, \delta\rho, \delta\dot{\rho}) \end{aligned} \tag{11}$$

where $\mathcal{I}$ is the 2-by-2 identity map of ρ and $\dot{\rho}$ perturbations and $\mathcal{M}_x$ includes the elements of $\mathcal{M}$ defining $\delta\mathbf{x}_i$. This last term is known to be the difference $\delta\bar{\mathbf{x}}_i$ between the candidate cataloged state and the reference ballistic one at the same epoch. As a consequence, $\mathcal{S}^{-1}$ map is evaluated in $\delta\bar{\mathbf{x}}_i$ so as to obtain the adjoint state at observation epoch $\boldsymbol{\lambda}_f$ as function of the only ρ and $\dot{\rho}$ perturbations. Plugging it in the state maps coming from the back-propagation flow $\mathcal{P}$ leads to the desired control profile and the corresponding expense $\Delta E(\delta\rho, \delta\dot{\rho})$ as defined in Eq. 2.

ADS and optimization

The objective of the optimization pipeline is to obtain the minimum optimal expense ΔE^* across the observables search space of interest for a candidate object.

ADS is used to split across ρ and $\dot{\rho}$ by fixing a maximum truncation error to ensure a reliable approximation of the thrust energy expense over the whole domain, at the expense of multiple propagations. In this regard, an a priori filtering step is performed to prevent an excessive increase in integration number. It consists in using the functions describing AR constraints throughout the iterative process to keep splitting the only subdomains compliant with boundary values of the semi-major axis (a_{min}, a_{max}) and eccentricity (e_{max}):

$$\begin{aligned} a(\rho, \dot{\rho}) - a_{max} &\leq 0 \\ a(\rho, \dot{\rho}) - a_{min} &\geq 0 \\ e(\rho, \dot{\rho}) - e_{max} &\leq 0 \end{aligned} \tag{12}$$

This is done by estimating the range bounds of each function within the current subdomain and enforcing Bolzano's theorem.

A similar selection process is applied as a posterior filtering step to keep the only subdomains containing stationary points, through gradient analysis: each of them complying with the required truncation error is scanned for null derivatives with respect to range and range-rate, being kept or discarded accordingly. This process does not directly relieve ADS computational burden, since derivatives are approximate polynomials stemming from the expansion, but represents a fundamental step of the optimization process.

A polynomial inversion is therefore performed on the gradient maps $\mathcal{G}$ defined in the selected subdomains so that the coordinates for each optimum can be retrieved as follows:

$$\begin{aligned} \begin{bmatrix} 0 \\ 0 \end{bmatrix} &= \mathcal{G}(\delta\rho, \delta\dot{\rho}) \\ \begin{bmatrix} \delta\rho \\ \delta\dot{\rho} \end{bmatrix} &= \mathcal{G}^{-1}(0, 0) \end{aligned} \tag{13}$$

In case $\delta\rho$ and $\delta\dot{\rho}$ values are outside the subdomain in which the map is defined, the stationary point is discarded. After a Hessian check to assess the stationary points type, the minima coordinates ρ^*, $\dot{\rho}^*$ and their magnitude ΔE^* are assigned to the candidate.

Uncertainty integration

Uncertainty flows in the process from the OCP boundary conditions and propagates throughout the whole pipeline, generating distributions of solutions. As for the catalog BC, in case a TLE is available, a covariance is usually computed according to the object orbital parameters ranges[12] while the acquired measurement uncertainty at observation epoch is derived from ground station accuracy data, usually expressed in terms of observables' standard deviation.

In order to propagate them to the ΔE^* solution and its ρ^*, $\dot{\rho}^*$ coordinates, TDA is exploited once again. Following the State Transition Tensor (STT) Theory[13] , the TPS coefficients used to approximate the non-linear transformations involved in the procedure can be used to obtain an N-th order expansion of the available covariances as the Jacobian projection does in the first order case.

To model uncertainty, these new polynomial maps have to be expanded around the nominal solutions retrieved in the previous section and the input state has to include the attributable perturbations $\delta\mathbf{a}$ so that its uncertainty can affect the output distribution as well. The procedure follows the same steps as the nominal case up to Eq. 13 with a selected expansion order of 3. The available mean and covariance are in this way propagated through the coefficients of the following TPSs:

$$\begin{aligned} \begin{bmatrix} \delta\rho \\ \delta\dot{\rho} \end{bmatrix} &= \mathcal{G}^{*^{-1}}(0, 0, \delta\mathbf{x}_i, \delta\mathbf{a}) \\ \Delta E &= \mathcal{E}^*(\delta\rho, \delta\dot{\rho}, \delta\mathbf{x}_i, \delta\mathbf{a}) \end{aligned} \tag{14}$$

Where $\mathcal{G}^{*^{-1}}$ links them to the minima coordinates while $\mathcal{E}^*$ to the corresponding expense.

Once the solution distribution is computed, the complete measurement vector $\mathbf{z}_f = (\rho, \dot{\rho}, \alpha, \delta, \dot{\alpha}, \dot{\delta})$ mean and covariance are back-propagated with a ballistic dynamics to the cataloged object epoch. A new TLE-derived covariance is assigned to the resulting state and the thrust energy distribution associated with the trajectory $\mathcal{N}(\Delta E_b, C_{\Delta E,b})$ is retrieved to be used as an approximate background expense related to the only BCs uncertainty.

Maneuver Detection

The obtained solution distribution can be used as a correlation metric on its own, identifying the RSO corresponding to the cheapest trajectory as the most likely correlation candidate. Nevertheless, a test to assess maneuver probability can be used to give contextual information on correlation. Two maneuver detection metrics are considered, so as to take two aspects of the maneuvering event into account: the underlying expense and the maneuver effect on the trajectory. As regards the former, the distributions involved in its formulation are converted from thrust energy to an equivalent approximate velocity expense, retrieved from Cauchy-Schwarz inequality:

$$\Delta V = \sqrt{2(t_f - t_i)\Delta E} \tag{15}$$

With this new index, not only is the effort weighed on the time distance between BCs, but the orders of magnitude involved are far more suitable to the detection process. The quantities involved are thus ΔV_{nom} being the solution for the nominal BCs case, the solution distribution $\mathcal{N}(\Delta V, C_{\Delta V})$ and the background ballistic one $\mathcal{N}_0(\Delta V_b, C_{\Delta V,b})$.

The first metric is computed by evaluating ΔV_{nom} in $\mathcal{N}_0$ Cumulative Distribution Function (CDF) to retrieve the probability that the nominal expense is higher than the uncertainty-derived one. $P_{MD} = \mathbb{P}(\Delta V \leq \Delta V_{nom})$ thus represents the confidence with which the nominal solution cannot be explained by the problem uncertainty. The $\mathcal{N}_0$ mean value ΔV_b represents the limitations imposed by BCs uncertainty and, as a consequence, the minimum detectable expense. The actual maneuver detection index is defined by amplifying every probability that is higher than 50% while putting to zero every value below this threshold to limit false positive cases:

$$P_{50} = \max(0, 2(P_{MD} - 0.5)) \tag{16}$$

This first metric is expected to be monitored together with an additional one based on the Squared Mahalanobis Distance (SMD) between the cataloged state at hand and the ballistic back-propagated one $\mathbf{x}_b$:

$$SMD(\mathbf{x}) = (\mathbf{x} - \mathbf{x}_b)^T (\mathbf{P}_x + \mathbf{P}_{x,b})^{-1} (\mathbf{x} - \mathbf{x}_b) \tag{17}$$

$SMD(\mathbf{x})$ can be directly compared with a n-variable $\chi^2_{n,c}$ distribution quantifying its distance through a predefined confidence level c (related to a σ factor distance from its mean), leading to the definition of the correlation index $P_{SMD} = SMD(\mathbf{x})/\chi^2_{n,c}$. The rationale for this metric lies in the fact that, following the optimal policy assumption, if the target BCs are connected by ballistic motion, the method is able to obtain a fairly accurate estimate of both post-maneuver state (from the minimum coordinates ρ, $\dot{\rho}$) and ΔE expense associated with the trajectory. Alternatively, in case the obtained solution diverges to a certain extent from the ballistic one (according to the involved uncertainties), it means that a control of some kind can be used to explain that difference. Consequently, P_{SMD} tries to quantifies this deviation, allowing for a better understanding of how much they can be mistaken. The main difference with respect to a standard correlation index resides in the space and epoch at which the distance is set up and in the uncertainties involved, avoiding TLE-derived uncertainty propagation and consequent over-inflation by relying more on sensor accuracy specifications. This provides an amplified SMD value for the same mean deviation due to the smaller inverted covariances involved, resulting in a stricter test.

RESULTS

In this section, several scenarios are used to test the algorithm's capability to perform correlation and maneuver hypothesis testing for the candidate object. They consist of an optical track (in the form of an attributable) sampled from a GEO object at different time spans from its last available orbital states. The target performs a different impulsive maneuver immediately after the cataloged epoch for each case. Their magnitude comprises values between 0 to $10\,m/s$, ranging from ballistic trajectory to high-thrust maneuvers. The focus lies on the method's effort distribution processing, but some considerations regarding its orbit determination capabilities are reported as well, to understand how this approach could suit that kind of task. The propagation is based on plain Keplerian dynamics, augmented with the OCP adjoint state. This simplification is deemed reasonable mostly because the method working principle does not rely on the kind of dynamics used: according to the fidelity requirements, a fully perturbed trajectory could be used as an expansion center of a purely Keplerian OCP expansion, or the expansion itself could embed a more accurate dynamics model. Moreover, due to the specific objective of the technique, the analyzed orbital regime, and the time span of interest, Keplerian motion is assumed to be a reliable first guess to identify correlation candidates. In any case, every unmodeled contribution used to generate the BCs would results in a parasitic term adding up to the expense.

As previously mentioned, while uncertainties associated with the candidate orbital state are computed for each scenario, assuming TLEs are used as orbital data, the measurement ones are fixed according to sensor accuracy. For the simulated scenarios, the selected sensor angles covariance comes from the French TAROT Calern ground station while the angular rates one is obtained by projecting the former across the time derivative computation step. The resulting orders of magnitude of the employed attributable standard deviation are $\sigma_{\mathbf{a}} = [1e-06\,\text{rad},\ 1e-06\,\text{rad},\ 1e-10\,\text{rad/s},\ 1e-07\,\text{rad/s}]$.

Ballistic trajectory case

The first scenario aims at assessing the method's performance when it comes to the correlation of an object following its ballistic trajectory without any maneuver being performed in the time

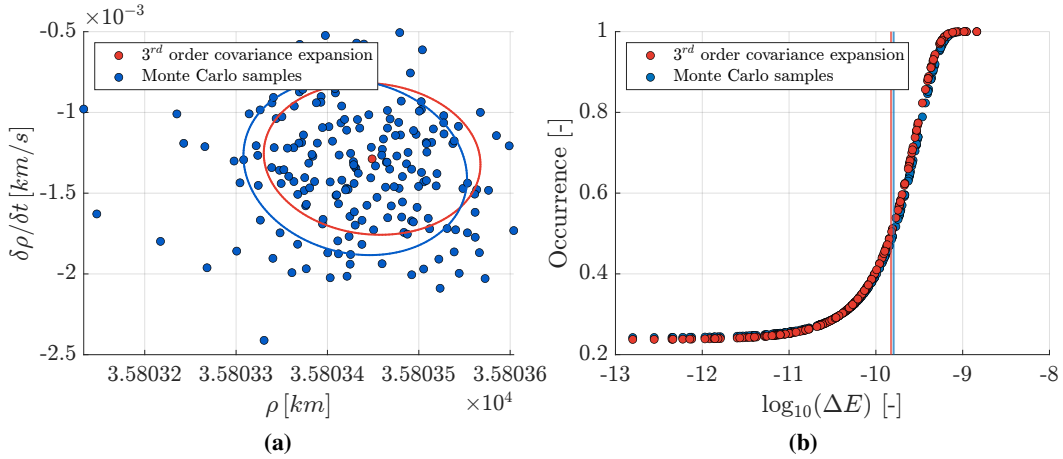

Figure 1: **Plot (a) shows a comparison between $\rho, \dot{\rho}$ Monte Carlo distribution (both displayed in blue) and the computed mean value and covariance (in red). In (b) a similar comparison between thrust energy expense CDFs is displayed.**

window of interest. The optical track acquisition is simulated at a fixed epoch, while the candidate state is sampled at a progressively prior epoch, with a time window spanning from 0.25 to 2 days. The GEO target orbit is defined by the following orbital parameters:

$$\mathbf{e}_{kep} = [42166\,\text{km},\ 4.18e-04,\ 0.14\,\text{deg},\ 68\,\text{deg},\ 235.5\,\text{deg}] \tag{18}$$

With true anomaly θ changing according to the selected candidate state. The corresponding state standard deviation changes as well according to the state but, to give a figure of its order of magnitude $\sigma_{\mathbf{x}_i} = [100\,\text{m},\ 100\,\text{m},\ 100\,\text{m},\ 0.1\,\text{m/s},\ 0.1\,\text{m/s},\ 0.1\,\text{m/s}]$.

The first of the performed tests consists in validating the normal assumption on both $\rho, \dot{\rho}$ and ΔE expense distributions and the choice of the order 3 expansion used in the uncertainty propagation section. Since the correlated object trajectories are in general expected to be close to a ballistic trajectory, the current scenario with BCs span $\Delta t = 2$ days is considered to be a reasonable first test for Gaussianity. To set up the comparison, a Monte Carlo simulation of 200 BCs is used to generate the reference distributions. They are thus standardized and a Kolmogorov-Smirnov hypothesis test is performed to assess if the samples can be identified as a normal distribution with a given level of significance (chosen as 5%). Both distributions pass the test as expected, due to the slow GEO dynamics and restrained non-linearity involved in the target integration time span. The following step consists in comparing the reference distributions with the ones given as output by the uncertainty propagation step of the algorithm. Comparing the resulting $\rho, \dot{\rho}$ distribution to the corresponding Monte Carlo, the SMD between them (0.0415) is well below the 1-σ distance (2.2173 for 2 degrees of freedom and $\sim 68\%$ confidence). The same happens for the SMD between ΔE distributions (0.0012 SMD value vs. 0.9372 value for 1 degree of freedom at 1-σ distance) so the two distributions are very close to being mistaken for the same one, as graphically shown in Figure 1.

As for the actual correlation and maneuver detection method validation, the procedure is organized as follows. The OCP is solved for every Δt (from 0.25 to 2 days) and the minimum expense

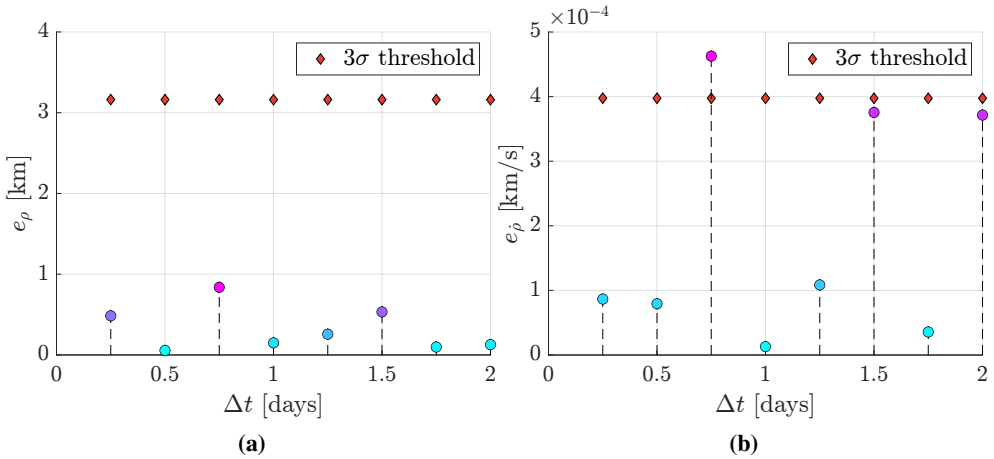

Figure 2: **Plot (a) shows the error values for ρ for every analyzed time span, while the one for $\dot{\rho}$ is displayed in plot (b). As expected by the ballistic case error magnitude is comparable with the 3-σ threshold of the solution coordinates distribution, represented by the diamond-shaped markers for every Δt.**

ΔE^* and $\rho^*, \dot{\rho}^*$ coordinates are obtained for every set of BCs. The corresponding distributions are therefore derived by recomputing the TPSs around the solutions to retrieve uncertainty.

Figure 2 shows the solution coordinates error with respect to the actual $\rho, \dot{\rho}$ values changing with the considered time span. As expected, since the optimal trajectory tends toward ballistic motion, the maneuver optimality hypothesis helps the correlation process in this case, leading in turn to a more reliable post-maneuver state estimate. Figure 3 shows how the thrust energy expense distributions seem to coincide no matter the time span, meaning a minimum value plateau due to the only BC uncertainty has been reached even for the shortest Δt considered. Moreover, this distribution systematically overestimates the actual expense associated with the impulsive maneuver (null in this instance) even in the nominal case, due to the minimum-energy formulation of the OCP and the low-thrust finite accelerations involved.

In this ballistic scenario, P_{50} is null for every time span due to the 50% threshold set to filter out false positives, so its values are not reported directly. Nonetheless, probability $P_{MD} = \mathbb{P}(\Delta V \leq \Delta V_{nom})$ together with correlation index P_{SMD} are displayed in Figure 4. A clear trend, similar to the one in $\rho, \dot{\rho}$ errors, can be noticed, reflecting the fact that uncertainty only is not enough to trigger P_{50} metric and, at the same time, the target would be correlated by P_{SMD} in any case.

Maneuvering case

The maneuvering cases consist of the simulation of different impulsive maneuvers, performed at the above-mentioned Δt distances (0.25 to 2 days) from the observation epoch. Maneuver intensity spans from -10 m/s to 10 m/s along Radial, Transverse, and Normal (RTN) components respectively, to carry out a sensitivity analysis to both maneuver magnitude, direction, and firing epoch. The solving process is identical to the one followed for the ballistic scenario.

The analysis of ρ and $\dot{\rho}$ errors is reported in Figure 5 for a series of radial, normal, and transverse maneuvers. In this maneuvering case, a further dimension is added to the plots, ranging across the

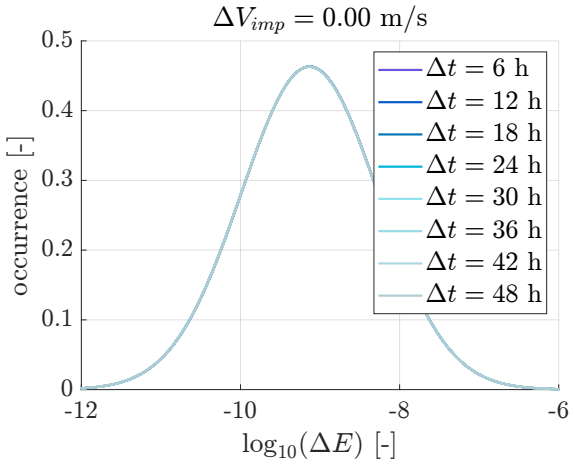

Figure 3: **The plot displays the thrust energy normal distributions associated with every Δt. They seem to coincide almost completely since the only factor driving their shape is the uncertainty level of the problem BCs.**

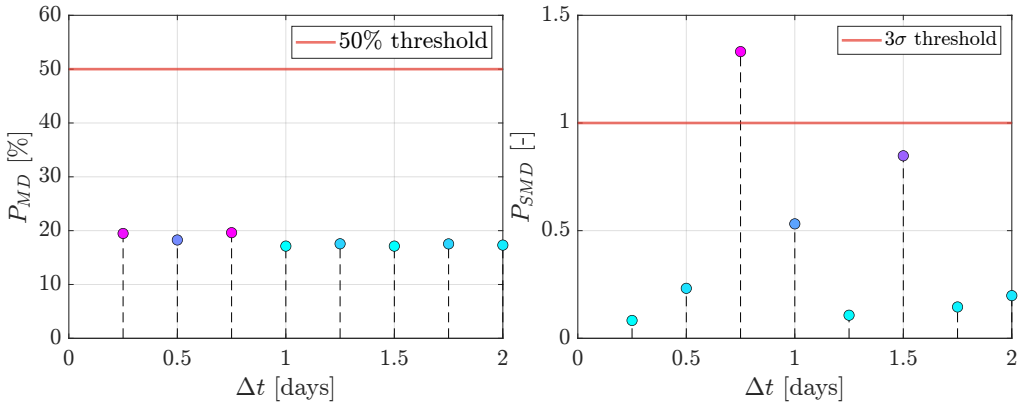

(a) **(b)**

Figure 4: **In plot (a) the values for P_{MD} are reported for every analyzed time span, with the minimum threshold for detection set to 50% (red horizontal line). Plot (b) shows the corresponding SMD-derived correlation index, the lower the more likely the object is correlated.**

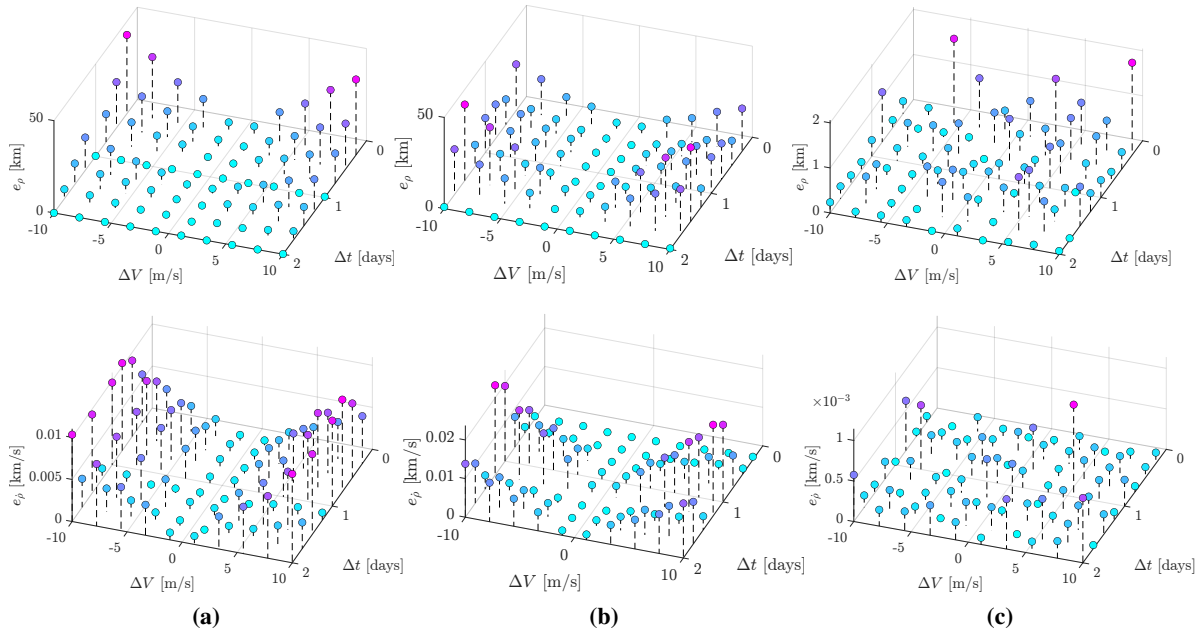

(a) **(b)** **(c)**

Figure 5: **The upper row shows ρ error values corresponding to every analyzed time span and maneuver magnitude for radial (a), transverse (b) and normal (c) maneuver direction. $\dot\rho$ errors are reported in the lower row instead. As expected, error magnitude decreases with decreasing ΔV magnitude (except for the normal case, showing generally lower errors).**

magnitude of the ΔV_{imp} component involved in the simulation. The xy plane of each graph spans the grid of all possible combinations of this last value with Δts. For radial maneuvers, since a larger time window between BCs allows for lower expenses, the trajectory becomes progressively close to the ballistic one with increasing Δt. The same happens with decreasing ΔV_{imp} magnitude, meaning that the OCP hypothesis becomes progressively closer to reality while diverging from the actual impulsive maneuver trajectory otherwise. For the transverse maneuver case, the same effect can be noticed in terms of ΔV_{imp} magnitude, but the trend is different in terms of Δt since changing the application point of a transverse impulsive maneuver can cause post-maneuver orbit changes of different intensity (this is the reason behind the sparse low error values across Δt in the radial maneuvers case as well). As a consequence, optimality weighs differently on the connection between the two orbits, causing the post-maneuver state to diverge from the impulsive solution. As for the normal one instead, the ΔV_{imp} magnitudes involved are low enough to allow the optimal trajectory not to get far from the ballistic one, leading to errors that are comparable to the ρ and $\dot\rho$ standard deviation order of magnitude.

In Figure 6 the thrust energy expense distributions for 24 of the simulated cases (3.33 m/s maneuver magnitude in the radial, transverse, and normal directions respectively, with different firing epochs) are reported, showing how the ΔE distribution shifts with different time spans, independently from the firing application point. As a higher Δt between BCs is available to perform an optimal maneuver, the thrust energy resulting from the OCP becomes progressively lower, flattening out on the uncertainty-only expense. The red vertical line in the plots represents the actual thrust energy solution retrieved from the impulsive ΔV_{imp} used to generate the maneuvers, always within the distribution despite being overestimated by the corresponding ΔV_{nom}, as in the ballistic case.

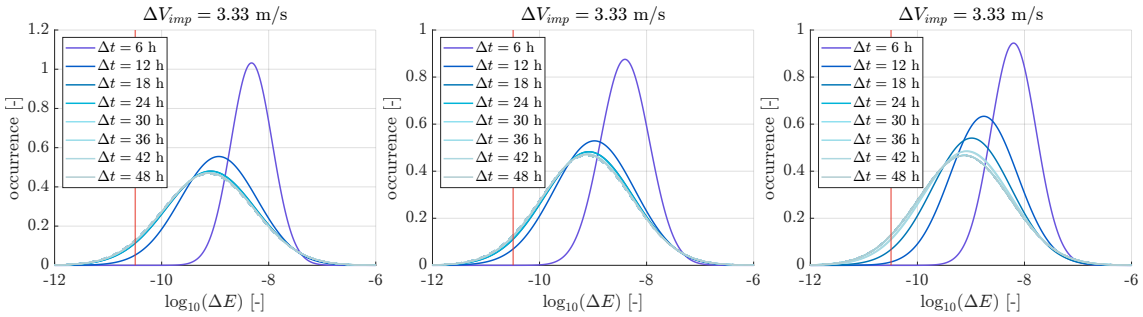

Figure 6: **The plot displays the thrust energy normal distributions associated with every Δt covering a radial (a), transverse (b), and normal (c) $3.33\,m/s$ magnitude maneuver. As Δt between BCs increases, a shift towards lower magnitudes is noticeable as progressively cheaper maneuvers are found as optimal solutions. The vertical red line represents the impulsive maneuver thrust energy, acting as a lower bound.**

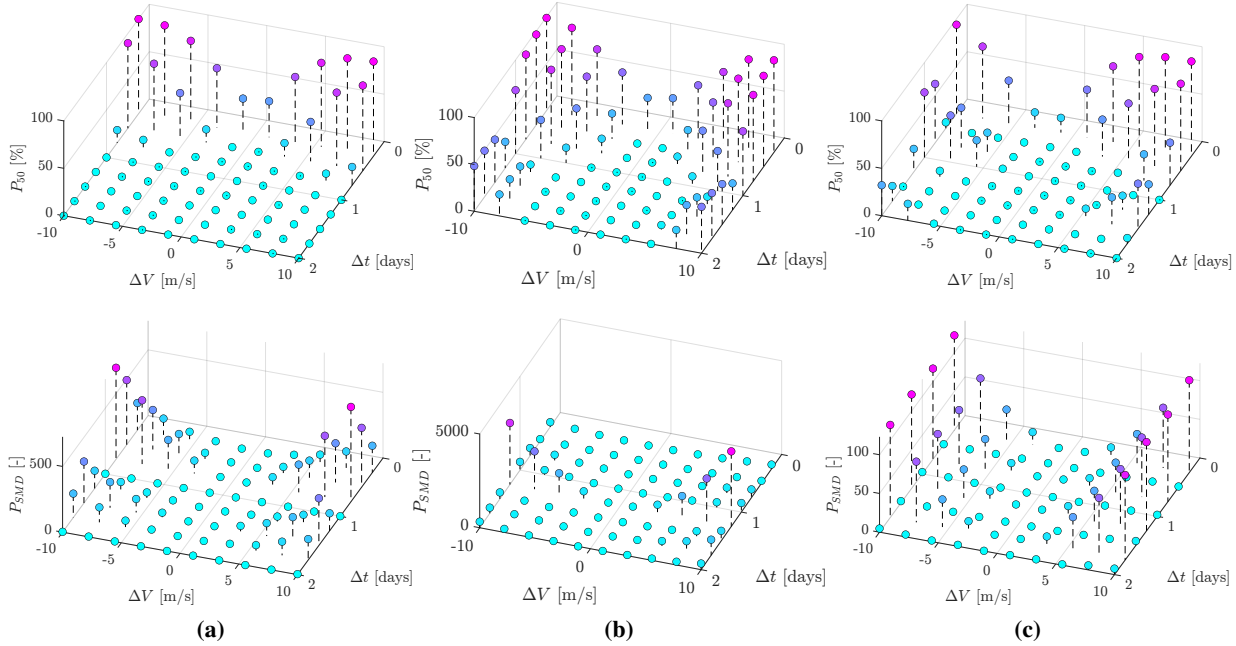

Figure 7: **In the upper row, P_{50} metric values are reported, covering every analyzed time span and maneuver magnitude for radial (a), transverse (b) and normal (c) maneuver direction. In the lower one the same results for correlation index P_{SMD} are displayed. The symmetry with respect to ΔV magnitude values highlights how complementary the two metrics are.**

Concerning the metrics, they are displayed in Figure 7. P_{50} metric achieves detection by overcoming the fixed 50% threshold on P_{MD}, namely when enough ΔV_{imp} is spent to perform the maneuver and the Δt available to the OCP forces it to increase the solution above the uncertainty-only expense level. On the other hand, while P_{SMD} mostly depends on ΔV_{imp} magnitude as well, some additional patterns can be noticed across Δt values. They are caused by changes in the impulsive maneuver application point, increasing or decreasing the deviation between pre- and post-maneuver orbits, and time span between BCs, generally mitigating the metric sensitivity to the firing epoch.

As a general remark, the two metrics can be seen as complementary, especially in an operational framework: an active spacecraft performing low-thrust maintenance maneuvers does not hinder standard correlation techniques such as P_{SMD} metric, since the energy-optimal trajectory is close to ballistic one enough to fall within its state distribution at the cataloged epoch. Only if a high enough thrust maneuver or several consecutive ones are performed without any acquisition in between, the distance between the distributions builds up so much that statistical distance-based correlation fails and OCP assumption starts to affect the result. In this case P_{50} metric comes into play to quantify the maneuver probability associated with every candidate, providing a reasonable first ranking of the most likely correlation candidates, while P_{SMD} provides a reliability check on P_{50}, allowing to understand how far from ballistic every optimal trajectory is: the higher its value the more significant P_{50} will be.

CONCLUSION

In this work, a novel method to integrate an optimal effort metric definition with a stricter SMD metric has been described as a robust way to perform correlation in an RSO catalog maintenance framework. A patchwork of Taylor polynomial expansions, ensuring a maximum truncation error, has been generated by means of an ADS technique to propagate a constrained AR back in time across the OCP integration flow. Uncertainty has been taken into account by propagating BCs distributions throughout the whole process to the target spaces. Two metrics have been formulated as an attempt for robust correlation supporting both frequent orbit maintenance low-thrust maneuvers and sparse high-thrust ones. Results state that these metrics are able to give a complete picture for every correlation candidate if used side by side. Current developments are aiming at integrating known objects orbital and maneuvering history as a further source of information, covering the lack of interaction between data-driven techniques and the maneuver optimality hypothesis, giving a first reasonable criterion to pick candidates.

REFERENCES

[1] E. S. D. Office, "Esa's Annual Space Environment Report," tech. rep., European Space Agency, April 2022.

[2] M. J. Holzinger, D. J. Scheeres, and K. T. Alfriend, "Object Correlation, Maneuver Detection, and Characterization Using Control Distance Metrics," *Journal of Guidance, Control, and Dynamics*, Vol. 35, July 2012, pp. 1312–1325, 10.2514/1.53245.

[3] A. Pastor, G. Escribano, and D. Escobar, "Satellite maneuver detection with optical survey observations," *Advanced Maui Optical and Space Surveillance Technologies Conference*, 2020.

[4] J. A. Siminski, H. Fiedler, and T. Flohrer, "Correlation of Observations and Orbit Recovery Considering Maneuvers," *AAS/AIAA Space Flight Mechanics*, 2017.

[5] A. Milani, G. F. Gronchi, M. D. M. Vitturi, and Z. Knežević, "Orbit determination with very short arcs. I admissible regions," *Celestial Mechanics and Dynamical Astronomy*, Vol. 90, Sept. 2004, pp. 57–85, 10.1007/s10569-004-6593-5.

[6] R. Serra, C. Yanez, and C. Frueh, "Tracklet-to-orbit association for maneuvering space objects using optimal control theory," *Acta Astronautica*, Vol. 181, Apr. 2021, pp. 271–281, 10.1016/j.actaastro.2021.01.026.

[7] K. J. DeMars, M. K. Jah, and P. W. Schumacher, "Initial Orbit Determination using Short-Arc Angle and Angle Rate Data," *IEEE Transactions on Aerospace and Electronic Systems*, Vol. 48, July 2012, pp. 2628–2637, 10.1109/TAES.2012.6237613.

[8] A. Wittig, P. Di Lizia, R. Armellin, K. Makino, F. Bernelli-Zazzera, and M. Berz, "Propagation of large uncertainty sets in orbital dynamics by automatic domain splitting," *Celestial Mechanics and Dynamical Astronomy*, Vol. 122, July 2015, pp. 239–261, 10.1007/s10569-015-9618-3.

[9] M. Berz and P. W. Hawkes, "Modern map methods in particle beam physics," *Advances in Imaging and Electron Physics*, Vol. 108, 1999, pp. 1–318.

[10] K. Makino and M. Berz, "Suppression of the Wrapping Effect by Taylor Model-based Validated Integrators," *International Journal of Pure and Applied Mathematics*, 2007.

[11] P. Di Lizia, R. Armellin, F. Bernelli-Zazzera, and M. Berz, "High order optimal control of space trajectories with uncertain boundary conditions," *Acta Astronautica*, Vol. 93, Jan. 2014, pp. 217–229, 10.1016/j.actaastro.2013.07.007.

[12] T. Flohrer, H. Krag, and H. Klinkrad, "Assessment and Categorization of TLE Orbit Errors for the US SSN Catalogue," *Advanced Maui Optical and Space Surveillance Technologies Conference*, 2008.

[13] K. Fujimoto, D. J. Scheeres, and K. T. Alfriend, "Analytical Nonlinear Propagation of Uncertainty in the Two-Body Problem," *Journal of Guidance, Control, and Dynamics*, Vol. 35, Mar. 2012, pp. 497–509, 10.2514/1.54385.